

Formation of an embryonic supermassive star in the first galaxy

Kohei Inayoshi^{1,2} ^{*}, Kazuyuki Omukai³ and Elizabeth Tasker⁴,

¹*Department of Physics, Graduate School of Science, Kyoto University, Kyoto 606-8502, Japan*

²*Department of Astronomy, Columbia University, 550 West 120th Street, New York, NY 10027, USA*

³*Astronomical Institute, Tohoku University, Sendai 980-8578, Japan*

⁴*Department of Physics, Faculty of Science, Hokkaido University, Sapporo 060-0810, Japan*

11 September 2018

ABSTRACT

We studied the gravitational collapse of a warm (~ 8000 K) primordial-gas cloud as a candidate progenitor for a supermassive star (SMS; $\gtrsim 10^5 M_\odot$) using a three-dimensional hydrodynamical simulation, including all the relevant cooling processes of both H_2 and H, which can potentially induce cloud fragmentation. This is the first simulation of this kind to resolve protostar formation. We find that the cloud undergoes runaway collapse without a major episode of fragmentation. Although the H_2 fraction jumps by a large factor via the three-body reaction at $\sim 10^{-13} \text{ g cm}^{-3}$, its cooling remains inefficient due to the optical thickness, and the temperature remains $\gtrsim 3000$ K. When the central core of the cloud becomes opaque to continuum radiation at $\sim 10^{-8} \text{ g cm}^{-3}$, a hydrostatic protostar with $\simeq 0.2 M_\odot$ is formed. The protostar grows to the mass $\simeq 1 M_\odot$ and the radius $\simeq 2$ AU within ~ 1 yr via rapid accretion of dense filamentary flows. With high accretion rate $\sim 2 M_\odot \text{ yr}^{-1}$, the protostar is expected to turn into a SMS within its lifetime, eventually collapsing to a seed for the supermassive black hole observed in the early Universe at $z \sim 7$.

Key words: cosmology: theory – dark ages, reionization, first stars – stars: formation – quasars: supermassive black holes

1 INTRODUCTION

Recent observations reveal the existence of supermassive black holes (SMBH) with masses $\gtrsim 10^9 M_\odot$ as early as redshift $z \gtrsim 7$ (e.g., Fan 2006; Mortlock et al. 2011). Their very existence puts a strong constraint on the origin and formation pathway of SMBHs, since the time required to form such massive objects from stellar-mass seed BHs ($\sim 100 M_\odot$) exceeds the then Hubble time. As a solution to this conundrum, the formation from massive seed BHs originating in the collapse of supermassive stars (SMSs; $\gtrsim 10^5 M_\odot$) has been suggested (e.g., Begelman et al. 2006). Seed BHs formed in this way are expected to grow to $\gtrsim 10^9 M_\odot$ by $z \sim 7$ via subsequent gas accretion (Di Matteo et al. 2012).

SMSs can be formed within primordial-gas clouds in massive halos with virial temperature $\gtrsim 10^4$ K, providing that H_2 cooling is prohibited throughout the protostellar collapse. Without this latter constraint, the gas would rapidly cool via H_2 and fragment into smaller pieces. The H_2 has to therefore be dissociated e.g., via the photodissociation by far-ultraviolet (FUV) radiation from nearby star-forming

galaxies (Omukai 2001; Bromm & Loeb 2003; Shang et al. 2010; Inayoshi & Omukai 2011) or the collisional dissociation in the shocked gas (Inayoshi & Omukai 2012). This in place, the cloud can collapse almost isothermally at ~ 8000 K solely by the H-atomic cooling. Previous numerical studies (e.g., Bromm & Loeb 2003; Wise et al. 2008; Shang et al. 2010) have implied that such a cloud collapses monolithically without efficient fragmentation. After a protostar is formed at the center, it then grows rapidly to a SMS via accretion from the envelope at a rate $\gtrsim 0.1 M_\odot \text{ yr}^{-1}$. Under such a high accretion rate, its growth is not hindered either by strong radiative feedback (Hosokawa et al. 2012, 2013) or by mass-loss due to stellar pulsations (Inayoshi et al. 2013).

So far, however, most studies (e.g., Regan & Haehnelt 2009; Latif et al. 2013b; Choi et al. 2013) have utilised several simplifying assumptions in studying the fragmentation process, e.g., turning off the H_2 cooling, adopting optically-thin treatment of $\text{Ly}\alpha$ cooling, or using insufficient chemical networks that neglect the H_2 formation. Yet the efficiency of fragmentation depends strongly on the thermal evolution determined by the cooling processes and chemical reactions. As a result, it still remains unresolved whether the cloud fragments during the isothermal collapse at ~ 8000 K be-

^{*} E-mail: inayoshi@astro.columbia.edu

fore forming the protostar. In this *Letter*, we use a three-dimensional hydrodynamical simulation to study the gravitational collapse of a turbulent primordial-gas cloud with mass $\gtrsim 10^5 M_\odot$. We follow the evolution until the formation of the protostar, including all relevant processes required for examining possible fragmentation during this collapse. Among these, the H_2 -line cooling is of primary importance due to its ability to rapidly drop the temperature via thermal instability if the gravitational collapse is delayed; a process possible due to turbulence generated during the virialization of the halo. If the thermal instability occurs, the cloud can fragment into many smaller mass clumps instead of forming a single SMS. We therefore simulate the collapse to determine the likelihood of the outcome being a monolithic collapse to a single star or fragmentation into a binary or multiple member system.

2 METHODOLOGY

We performed a three-dimensional hydrodynamical simulation of the gravitational collapse of a primordial-gas cloud using the adaptive mesh refinement (AMR) code, **ENZO** (Bryan et al. 2014). Our main purpose is to investigate the gas dynamics over a wide range of the densities ($10^{-21} \lesssim \rho \lesssim 10^{-7} \text{ g cm}^{-3}$). The cloud initially has a spherically symmetric density profile enhanced by a factor f ($= 1.6$) above the critical Bonnor-Ebert (BE) distribution; an isothermal sphere supported in marginal hydrostatic equilibrium against gravitational collapse. According to cosmological simulations (e.g., Wise et al. 2008), at the center of a first galaxy with virial temperature $\gtrsim 10^4 \text{ K}$, forming in an environment where the H_2 formation is suppressed, a warm ($T \sim 8000 \text{ K}$) cloud with $\sim 10^5 M_\odot$ becomes gravitationally unstable at $\rho \sim 10^{-20} \text{ g cm}^{-3}$ and collapses. Based on this, we set the central density and temperature of the cloud to $\rho_c = 1.67 \times 10^{-20} \text{ g cm}^{-3}$ and $T = 8000 \text{ K}$, giving a mass and radius of $1.17 \times 10^5 M_\odot$ and 10.8 pc , respectively. Although we here do not impose an external FUV radiation, H_2 is collisionally dissociated for $\rho \gtrsim 10^{-20} \text{ g cm}^{-3}$ and $T \gtrsim 6000 \text{ K}$. Note that we neglect the dark-matter gravity since the cloud is already bound by the self-gravity of its gas. Our simulation box size is $(50 \text{ pc})^3$ and refinement is controlled by insisting that one Jeans length is resolved by at least 64 grid cells (e.g., Turk et al. 2012). Under this condition, the simulation uses 23 out of the allowed 25 refinement levels, ensuring we are resolved by the above criteria at all times and giving a limiting resolution of $\lesssim 0.1 \text{ AU}$.

The development of turbulence in the central region of forming first galaxies has been suggested by numerical simulations (e.g., Wise & Abel 2007; Greif et al. 2008). In the initial phase of collapse with $\sim 10^{-20} \text{ g cm}^{-3}$, the turbulence is still subsonic in the cloud. To consider the density and velocity perturbations due to the turbulence, we initially impose a subsonic velocity field (the root mean square of the velocity is set to $0.1 c_s$) with power spectrum $P(k) \propto k^{-4}$, which corresponds to the so-called Larson’s law for the contemporary star-forming regions (Larson 1981). To ensure the turbulence adequately resolved, we select the maximum k-mode value of $1/10$ of the number of cells across the cloud.

We consider the non-equilibrium primordial chemistry of 9 species (H , H_2 , e^- , H^+ , H_2^+ , H^- , He , He^+ , and He^{++})

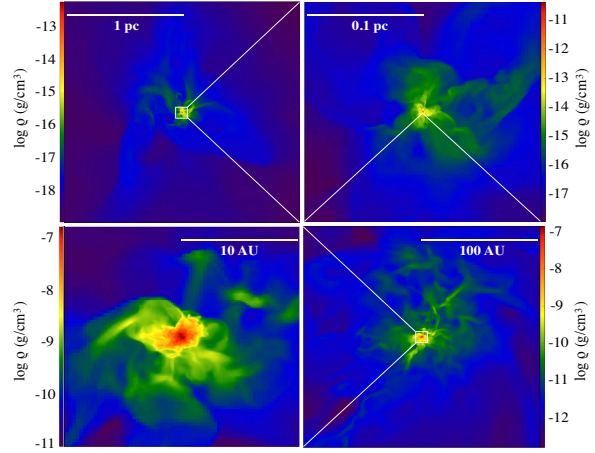


Figure 1. Density distribution in the plane through the density peak for four spatial scales: from top-left, clockwise: the large-scale gas distribution ($\sim 1 \text{ pc}$), a collapsing core by the H^- free-bound continuum cooling ($\sim 0.1 \text{ pc}$), the central region around the protostar ($\sim 100 \text{ AU}$), and the final protostar ($\sim 10 \text{ AU}$).

and 13 hydrogen reactions selected to reproduce the correct thermal/chemical evolution of the warm atomic-cooling cloud (reactions 3, 4, 7–10, 12, 15–18, 28, and 32 in Table. 2 of Omukai 2001). We adopt the reaction rate coefficients updated by the following studies: 7–10 (Coppola et al. 2011), 15 (Martin et al. 1996), 17 (Stibbe & Tennyson 1999), and 28 (Ferland et al. 1992). The 4 helium reactions originally included in **ENZO** are also present, although they are not relevant in our calculation. We initially assume a uniform distribution of ionization degree with 10^{-4} and H_2 molecular fraction with 10^{-7} , respectively (e.g., Shang et al. 2010). At high density, the chemical reactions proceed faster than the cloud collapse and chemical equilibrium is achieved. To smoothly connect the non-equilibrium chemistry to that of equilibrium, we solve the chemical network including both the forward and reverse reactions for dominant processes. To solve the chemistry equations, we employ the piecewise exact solution method (Inoue & Inutsuka 2008) instead of the original **ENZO** solver. For the radiative cooling, we consider atomic cooling ($H \text{ Ly}\alpha$, two photon emission, and H^- free-bound, free-free emission) and H_2 cooling (rovibrational line and collision-induced emission). We also include the suppression of the cooling rate in the optically thick case by using the optical depth estimated as $\rho \kappa_R L_c$ (e.g., Omukai 2001; Shang et al. 2010), where κ_R is the Rosseland mean opacity considering the H_2 Rayleigh scattering, the H_2 collision-induced absorption, and the H^- bound-free and free-free absorption, and L_c the size of the central core, which is approximately given by the Jeans length for the spherically symmetric cloud in the runaway collapse.

3 RESULTS

Fig. 1 shows the density distribution at the end of the simulation, where the central density reaches $\sim 10^{-7} \text{ g cm}^{-3}$, for four different spatial scales; from the top-left clockwise, large-scale gas distribution ($\sim 1 \text{ pc}$), the collapsing core ($\sim 0.1 \text{ pc}$), the central $\sim 100 \text{ AU}$ region, and the protostar formed at the center ($\sim 10 \text{ AU}$). The central portion of

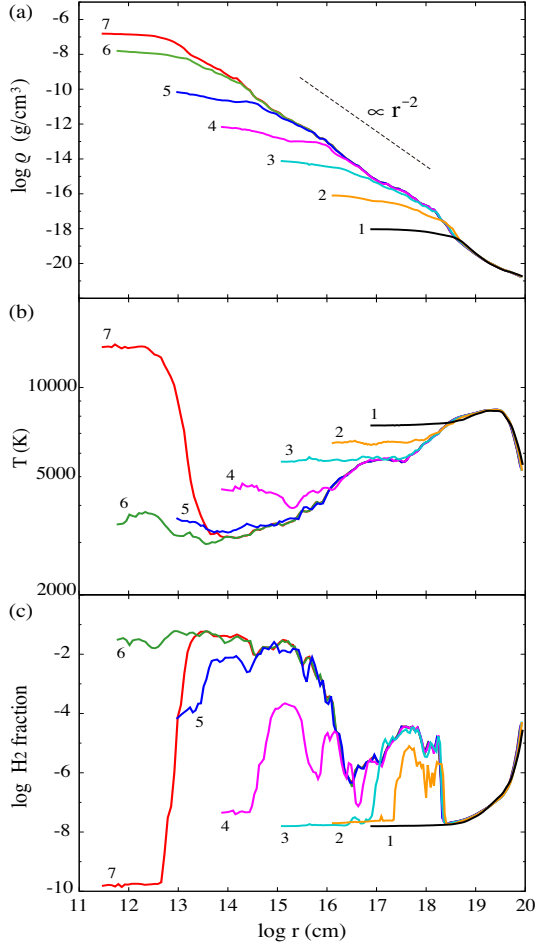


Figure 2. Mass-weighted radial profiles at different evolutionary stages of (a) mass density, (b) temperature, and (c) H_2 fraction. The time sequences are indicated by numbers: (1) 8.0×10^5 yr after the initial state of our simulation. (2) 9.3×10^4 yr after (1): the main coolants are the $\text{Ly}\alpha$ and two-photon emissions. (3) 1.6×10^4 yr after (2): dominant cooling process shifts to the H^- free-bound emission in the central core. (4) 1.8×10^3 yr after (3): H_2 formation via the three-body reaction becomes active at the centre. (5) 2.8×10^2 yr after (4): the cloud becomes optically thick to dominant H_2 lines. (6) 1.8×10^1 yr after (5): the cloud becomes optically thick to the continuum opacities and a hydrostatic core is formed at the centre. (7) 1.2 yr after (6): the final state of the simulation.

the cloud undergoes the runaway collapse. The turbulence forms filamentary structures that channel material into the central region ($\rho \sim 10^{-8} \text{ g cm}^{-3}$), feeding the protostar. The left-bottom panel presents the density distribution around the protostar. At the end of this simulation, the protostellar mass reaches $\simeq 1 M_\odot$ and its radius $\simeq 2 \text{ AU}$. These values are consistent with the result of the stellar-structure calculation by Hosokawa et al. (2012), who assumed a steady and spherical accretion.

Fig. 2 shows the evolution of mass-weighted radial profiles of (a) density, (b) temperature, and (c) H_2 fraction. During collapse, the density profile obeys the self-similar solution, which consists of the central core with flat density distribution and envelope with the $\rho \propto r^{-2}$ law (e.g., Larson 1969). The central core collapses almost isothermally until

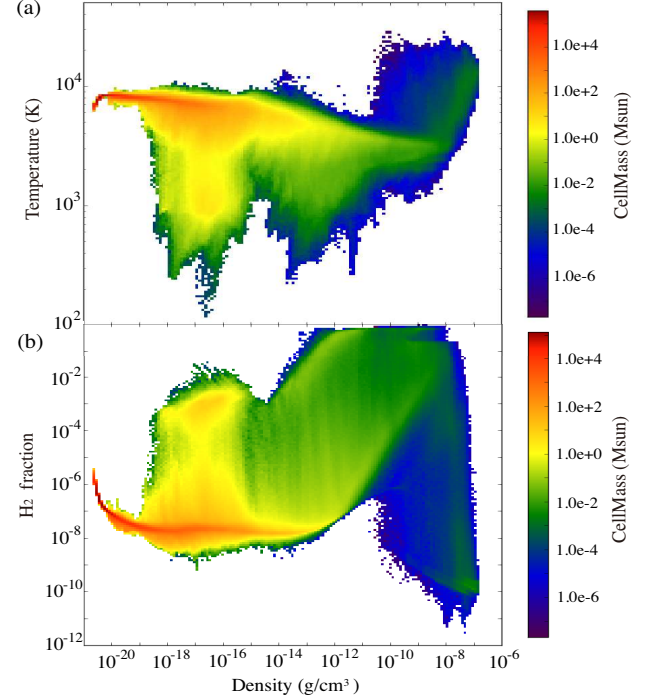


Figure 3. Phase diagrams showing the distribution of (a) density-temperature and (b) density- H_2 fraction of the collapsing cloud at the end of the simulation. The colors represent the total mass at the respective density and temperature.

$\sim 10^{-8} \text{ g cm}^{-3}$ keeping the temperature at $\sim 5000 \text{ K}$. In the low density regime of $\rho < 10^{-16} \text{ g cm}^{-3}$, the cooling is mainly via the $\text{H Ly}\alpha$ and two-photon emission. At higher density, the dominant cooling process shifts to the H^- free-bound emission ($\text{H} + \text{e}^- \rightarrow \text{H}^- + \gamma$). For $\gtrsim 10^{-9} \text{ g cm}^{-3}$, photons from the H^- free-bound emission are self-absorbed, as well as Rayleigh scattered by the H_2 . The gas cools further by the H^- free-free emission ($\text{H} + \text{e}^- \rightarrow \text{H} + \text{e}^- + \gamma$) until $\gtrsim 10^{-8} \text{ g cm}^{-3}$. Finally, the cloud becomes opaque to all those continuum opacities at $\sim 10^{-8} \text{ g cm}^{-3}$ and a hydrostatic core, i.e., a protostar, with its mass $\simeq 0.2 M_\odot$ and radius $\simeq 1 \text{ AU}$ is formed at the center, where the core temperature is $\sim 4000 \text{ K}$. As the protostar grows to $\sim 1 M_\odot$, the temperature inside the protostar adiabatically increases to $\sim 10^4 \text{ K}$.

The mass-weighted H_2 fraction initially approaches the equilibrium value ($\sim 10^{-8}$), where the formation through the electron-catalyzed reaction ($\text{H} + \text{e}^- \rightarrow \text{H}^- + \gamma$; $\text{H}^- + \text{H} \rightarrow \text{H}_2 + \text{H}$) and the collisional dissociation ($\text{H}_2 + \text{H} \rightarrow 3\text{H}$) are balanced. At $\rho \gtrsim 10^{-13} \text{ g cm}^{-3}$, the H_2 fraction jumps up to ~ 0.1 by the three-body reaction ($3\text{H} \rightarrow \text{H}_2 + \text{H}$) in the inner region ($r \lesssim 10^3 \text{ AU}$). However, neither the H_2 line nor collision-induced-emission (CIE) cooling plays a significant role in the thermal evolution: H_2 lines are optically thick for $\rho \gtrsim 10^{-10} \text{ g cm}^{-3}$ and other continuum cooling is more important than the H_2 CIE cooling. After the protostar formation, the H_2 is dissociated inside owing to the high temperature.

Fig. 3 presents the phase diagrams showing the distribution of (a) temperature and (b) H_2 fraction as a function of the density at the end of the simulation. The cloud consists

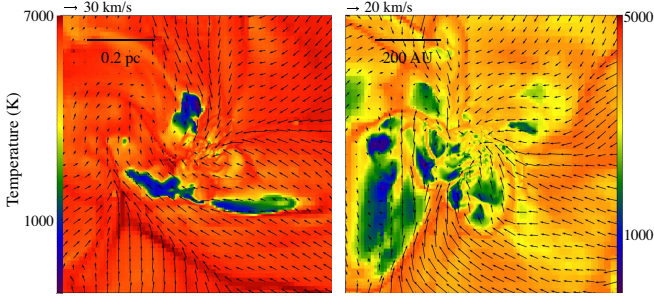


Figure 4. Temperature (color) and velocity field (arrows) in the plane through the density peak for two spatial scales. Cold regions are formed by the chemo-thermal instabilities due to the H_2 formation by the electron-catalyzed reaction (left) and by the three-body reaction (right).

of two thermal phases of the gas, i.e., hot (\sim several 10^3 K) and cold ($\sim 10^3$ K) components. As seen in Figs. 2(b) and 3(a), most of the collapsing gas resides in the hot component, which ultimately forms a protostar at the center. Note that since the density profile follows the self-similar form during the runaway collapse and thus the radial position has one-to-one correspondence with the density (Fig. 2a), the density-temperature distribution of the hot component is just a reflection of the temperature profile (Fig. 2b). The H_2 fraction in the hot component remains almost constant at $\sim 10^{-8}$ up to 10^{-13} g cm $^{-3}$ and then increases almost proportionally to the density for higher density by the three-body reaction until finally dissociated at $\gtrsim 10^{-8}$ g cm $^{-3}$ as a result of the protostar formation.

Meanwhile, the cold component exists over the wide density range, $10^{-18} \lesssim \rho \lesssim 10^{-11}$ g cm $^{-3}$. This gas is produced by the thermal instability induced by the combination of the adiabatic cooling due to the turbulent expansion and the subsequent H_2 cooling. Once the temperature decreases via adiabatic cooling, the H_2 dissociation becomes inefficient, enhancing the H_2 fraction and its cooling rate, causing the temperature to plummet. This process is known as the chemo-thermal instability associated with the H_2 formation/dissociation (Yoshii & Sabano 1979; Silk 1983).

Fig. 4 presents the temperature distribution and velocity fields for two different scales. In both panels, the coexistence of the cold and hot components is clearly visible. Turbulence establishes a complex structure of interacting shocks and stagnation points. The cold components in the two scales are produced by the thermal instabilities due to the H_2 formation through the electron-catalyzed reaction (~ 0.2 pc) and three-body reaction (~ 200 AU) (see also Fig. 3b). The cold components are not massive enough to be gravitationally bound and have no influence on the evolution of the central collapsing region.

Fig. 5 presents the profiles of the radial and tangential velocities. Also shown for comparison is half of the Keplerian velocity and the sound speed. Both the radial and tangential flows become supersonic with the Mach number of 2–3. At the surface of the protostar, the radial flow is abruptly brought to a halt. In the accreting envelope, the tangential velocity is as large as half the Keplerian velocity, in accordance with previous studies of Pop III star formation (e.g., Abel et al. 2002; Yoshida et al. 2008). It is known

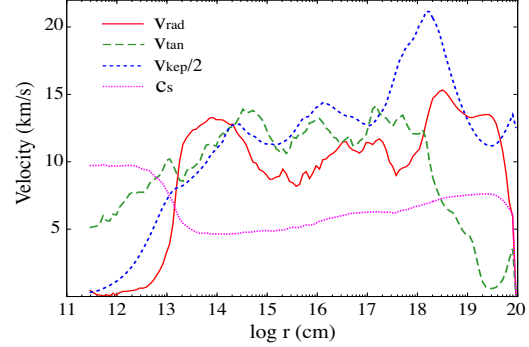


Figure 5. Profiles of the radial (solid) and tangential velocities (long-dashed) at the end of the simulation. For comparison, a half of the Keplerian velocity (short-dashed) and sound speed (dotted) are also shown. All the quantities are spherically averaged.

that the cloud can contract in the runaway fashion even with conserved angular momentum as long as the temperature does not increase with the density (e.g., Narita et al. 1984; Saigo & Hanawa 1998). After protostar formation, on the other hand, materials initially located in the outer radius and thus with higher specific angular momentum begin to fall in, and the centrifugal radius increases outward (Saigo et al. 2000). In our simulation, however, the rotationally supported disk has not yet appeared because the centrifugal radius ($\lesssim 0.1$ AU; McKee & Tan 2008) is still smaller than the stellar radius ~ 1 AU in this early accretion phase.

Fig. 6 shows the radial profile of the mass infall rate as a function of the enclosed mass. This can be regarded as the temporal evolution of the accretion rate after the protostar formation. Note that the value inside the protostar ($M_r \lesssim 1 M_\odot$) is not equivalent to the accretion rate. The infall rate becomes almost constant for the flat temperature profile because in the self-similar solution, the flat temperature profile is proportional to c_s^3/G , which depends only on the temperature of the accreting envelope. The typical value is as high as $\sim 2 M_\odot \text{ yr}^{-1}$, which is consistent with the previous simulations starting from the cosmological initial condition (e.g., Latif et al. 2013b). This infall rate is larger than $20 c_s^3/G$ for $T = 8000$ K and similar to the value found for the runaway collapse starting from an initial condition not so far from the hydrostatic equilibrium. (Foster & Chevalier 1993). The protostar is expected to grow via such rapid accretion to a SMS within its lifetime $\sim 10^6$ yr. When the stellar mass exceeds $\sim 10^5 M_\odot$, the SMS is expected to collapse to a BH by the general relativistic instability (Chandrasekhar 1964; Hosokawa et al. 2013).

4 CONCLUSION AND DISCUSSION

We have performed numerical simulation of the collapse of a massive ($\gtrsim 10^5 M_\odot$) and warm (~ 8000 K) primordial-gas cloud. We have found that the cloud collapses almost isothermally by the H atomic cooling and does not experience major episode of fragmentation in spite of the presence of turbulence. Finally, a small protostar with mass $\sim 0.2 M_\odot$ is formed when the central part becomes optically thick to the continuum radiation at $\rho \gtrsim 10^{-8}$ g cm $^{-3}$, and grows to

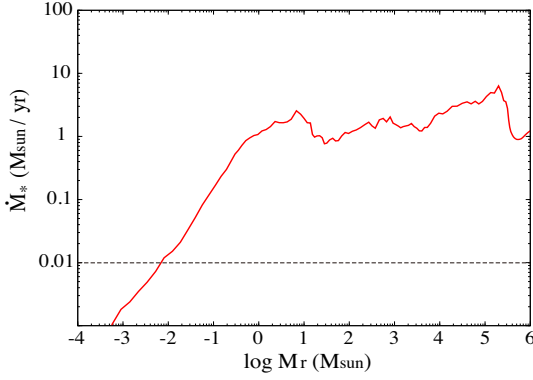


Figure 6. Profile of the mass infall rate ($\dot{M}_* = -4\pi r^2 v_{\text{rad}}$) as a function of the enclosed mass at the end of the simulation. The horizontal line indicates the critical value $10^{-2} M_\odot \text{ yr}^{-1}$, above which the protostar swells to supergiant and the radiative feedback is strongly suppressed. (Hosokawa et al. 2012).

the mass $\simeq 1 M_\odot$ and radius $\simeq 2 \text{ AU}$ by the end of the simulation.

The protostar, once formed, grows via rapid accretion of the dense filamentary flows at an approximately constant rate $\sim 2 M_\odot \text{ yr}^{-1}$. In cases with accretion rate higher than $10^{-2} M_\odot \text{ yr}^{-1}$ (dashed line in Fig. 6), the protostar is known to develop a giant-like structure (“supergiant” protostar) with a bloated stellar envelope and contracting central core (Hosokawa et al. 2012, 2013). Since the effective temperature of such a supergiant protostar is $\lesssim 10^4 \text{ K}$, the UV feedback is unlikely to prevent the mass accretion onto the star. Although a supergiant protostar is unstable to the stellar pulsations by the κ -mechanism, the resultant mass-loss rate is much lower than the accretion rate (Inayoshi et al. 2013). After the protostar grows to a SMS ($\gtrsim 10^5 M_\odot$) via rapid accretion, it eventually collapses through the general relativistic instability to turn into a seed of high- z SMBHs (e.g., Fan 2006; Mortlock et al. 2011).

In this *Letter*, we have started the calculation from the initial condition of a critical BE sphere with turbulence, and have found a single protostar formed without a major episode of fragmentation. Since at $\lesssim 0.1 \text{ pc}$ the profiles of the density and tangential velocity converge to self-similar forms with $\rho \propto r^{-2}$ and $v_{\text{tan}} \simeq 0.5 v_{\text{Kep}}$, independent of the initial conditions (Figs. 2a and 5), we expect that our conclusions depend only weakly on the initial setup.

In this simulation, we have neglected the effect of magnetic fields. Previous studies suggest that magnetic field strength could rival that of the turbulent energy (e.g., Federrath et al. 2011; Turk et al. 2012; Latif et al. 2013a) with the effect of either increasing accretion efficiency (via magnetic breaking producing a more spherical flow) or decreasing it via protostellar jets (Machida et al. 2006). This exploration will be left for future investigations.

ACKNOWLEDGEMENTS

We thank the Enzo and yt support teams, especially Brian O’Shea and Matthew Turk for their useful advice. We also thank Takashi Nakamura, Takashi Hosokawa, Naoki Yoshida, Shu-ichiro Inutsuka, Tsuyoshi Inoue, and Kei

Tanaka for their fruitful discussions. Numerical computations were carried out on the Cray XC30 at the Center for Computational Astrophysics of the National Astronomical Observatory of Japan. This work is supported in part by the Grants-in-Aid by the Ministry of Education, Culture, and Science of Japan (KI 23-838; KO 21684007, 25287040).

REFERENCES

- Abel, T., Bryan, G. L., & Norman, M. L. 2002, *Science*, 295, 93
 Begelman, M. C., Volonteri, M., & Rees, M. J. 2006, *MNRAS*, 370, 289
 Bromm, V., & Loeb, A. 2003, *ApJ*, 596, 34
 Bryan, G. L., Norman, M. L., O’Shea, B. W., et al. 2014, *ApJS*, 211, 19
 Chandrasekhar, S. 1964, *ApJ*, 140, 417
 Choi, J.-H., Shlosman, I., & Begelman, M. C. 2013, *ApJ*, 774, 149
 Coppola, C. M., Longo, S., Capitelli, M., Palla, F., & Galli, D. 2011, *ApJS*, 193, 7
 Di Matteo, T., Khandai, N., DeGraf, C., et al. 2012, *ApJL*, 745, L29
 Fan, X. 2006, *New Astron. Rev.*, 50, 665
 Federrath, C., Sur, S., Schleicher, D. R. G., Banerjee, R., & Klessen, R. S. 2011, *ApJ*, 731, 62
 Ferland, G. J., Peterson, B. M., Horne, K., Welsh, W. F., & Nahar, S. N. 1992, *ApJ*, 387, 95
 Foster, P. N., & Chevalier, R. A. 1993, *ApJ*, 416, 303
 Greif, T. H., Johnson, J. L., Klessen, R. S., & Bromm, V. 2008, *MNRAS*, 387, 1021
 Hosokawa, T., Omukai, K., & Yorke, H. W. 2012, *ApJ*, 756, 93
 Hosokawa, T., Yorke, H. W., Inayoshi, K., Omukai, K., & Yoshida, N. 2013, *ApJ*, 778, 178
 Inayoshi, K., & Omukai, K. 2011, *MNRAS*, 416, 2748
 Inayoshi, K., & Omukai, K. 2012, *MNRAS*, 422, 2539
 Inayoshi, K., Hosokawa, T., & Omukai, K. 2013, *MNRAS*, 431, 3036
 Inoue, T., & Inutsuka, S.-i. 2008, *ApJ*, 687, 303
 Larson, R. B. 1969, *MNRAS*, 145, 271
 Larson, R. B. 1981, *MNRAS*, 194, 809
 Latif, M. A., Schleicher, D. R. G., Schmidt, W., & Niemeyer, J. 2013a, *MNRAS*, 432, 668
 Latif, M. A., Schleicher, D. R. G., Schmidt, W., & Niemeyer, J. 2013b, *MNRAS*, 433, 1607
 Machida, M. N., Omukai, K., Matsumoto, T., & Inutsuka, S.-i. 2006, *ApJL*, 647, L1
 Martin, P. G., Schwarz, D. H., & Mandy, M. E. 1996, *ApJ*, 461, 265
 McKee, C. F., & Tan, J. C. 2008, *ApJ*, 681, 771
 Mortlock, D. J., et al. 2011, *Nature*, 474, 616
 Narita, S., Hayashi, C., & Miyama, S. M. 1984, *Progress of Theoretical Physics*, 72, 1118
 Omukai, K. 2001, *ApJ*, 546, 635
 Regan, J. A., & Haehnelt, M. G. 2009, *MNRAS*, 396, 343
 Saigo, K., & Hanawa, T. 1998, *ApJ*, 493, 342
 Saigo, K., Matsumoto, T., & Hanawa, T. 2000, *ApJ*, 531, 971
 Shang, C., Bryan, G. L., & Haiman, Z. 2010, *MNRAS*, 402, 1249
 Silk, J. 1983, *MNRAS*, 205, 705
 Stibbe, D. T., & Tennyson, J. 1999, *ApJL*, 513, L147
 Turk, M. J., Oishi, J. S., Abel, T., & Bryan, G. L. 2012, *ApJ*, 745, 154
 Wise, J. H., & Abel, T. 2007, *ApJ*, 665, 899
 Wise, J. H., Turk, M. J., & Abel, T. 2008, *ApJ*, 682, 745
 Yoshida, N., Omukai, K., & Hernquist, L. 2008, *Science*, 321, 669
 Yoshii, Y., & Sabano, Y. 1979, *PASJ*, 31, 505